Theory of magnetized, coupled, rf-driven plasma sheaths in one dimension

Spilios Riyopoulos
Science Applications International Corporation, McLean, Virginia 22102
(Received 29 January 1998; revised manuscript received 28 September 1998)

A set of equations for magnetized plasma sheaths in rf capacitance discharges is developed within the adiabatic electron, fluid ion framework. It differs from previous approaches in that (a) ion demagnetization, i.e., the detachment of the ion flow from the magnetic lines caused by electrostatic gradients, is introduced self-consistently, (b) the ion injection velocity from the presheath is reevaluated to ensure the ion-electron flux balance, and (c) two symmetrically opposed coupled sheaths are driven by a sinusoidal driving voltage instead of a sinusoidal current. It is found that the sheath potential and thickness increase considerably with increasing magnetic inclination θ relative to the electric field compared to the unmagnetized results; the latter are recovered at the parallel magnetic field limit. Also, the ion injection velocity along the magnetic lines is subsonic and depends on the magnetic inclination. Finally, a sinusoidal ac voltage drives an anharmonic sheath current, while a sinusoidal current drives anharmonic voltage. [S1063-651X(99)09001-7]

PACS number(s): 52.40.Hf, 52.80.Pi, 52.20.Dq

I. INTRODUCTION

A plasma sheath is a charged boundary layer formed at plasma-boundary interfaces because of the difference in mobility among the various charge carriers. Electron depletion, due to the electrons' higher mobility, leaves a positively charged ion column. The ensuing potential gradient tends to slow down the electrons and accelerate the ions until a steady state is reached with equal ion and electron fluxes. Sheath formation in plasmas externally driven at high rf power, where the applied (or induced) voltage is much stronger than the thermal potential of the ambient plasma, is of interest in applications ranging from plasma processing reactors to ion cyclotron heating of fusion plasmas. Usually the extent of the sheath is much shorter than the applied rf wavelength so that electric field variations matter only in one dimension, across the sheath. A one-dimensional, ''moving plate capacitor'' model has been developed [1,2] to describe sheath formation in rf-driven capacitor discharges when the sheath thickness is much smaller than the sheath length. The sheath equations are based on the assumption of adiabatic electrons, in thermal equilibrium with the instantaneous sheath potential, and fluid ions, responding to the time-averaged sheath field.

More often than not, a significant magnetic field is present at an angle to the electric field. Studies of magnetic effects on *static* (thermal) plasma sheaths [3] showed a significant effect of the magnetic angle on the magnetized plasma presheath. Surprisingly, earlier treatments [4,5] of rf-driven sheaths, assuming small Larmor radius magnetized ions with motion constrained along the magnetic lines, yielded sheath scaling that is independent of the magnetic inclination, contrary to numerical results [6] showing a strong dependence.

It has been since shown [7] that the presence of an electrostatic gradient oblique to the magnetic field allows cross-B ion drift in the direction of the transverse electric field $\mathbf{E}_\perp$ in addition to the usual $\mathbf{E}\times\mathbf{B}$ drift under uniform $\mathbf{E}$. The ion flow detaches from the magnetic lines, pointing closer to the direction of the electric field than the magnetic angle θ (Fig. 1) as a consequence of the guiding center drift. The Larmor radius remains much smaller than the sheath thickness and is treated as an adiabatic invariant. As the magnetized presheath ions become partially demagnetized in a strong sheath E gradient, a new effective mass m^* applies for the reduced one-dimensional (1D) equation of motion along $\mathbf{E}$. In the present formalism, the effective ion mass is allowed to vary self-consistently across the sheath since the ion flow angle θ^* changes with the local electric gradient dE/dx. An earlier treatment [6], addressing the sheath scaling observed in numerical simulations, used a constant effective mass, taking the asymptotic limit of the ion drift in a quadratic effective sheath potential.

This paper addresses the magnetic effects by (i) incorporating the cross-magnetic ion flow in a self-consistent 1D model, (ii) applying a sinusoidal voltage, rather than current through the sheath, as the boundary condition, and (iii) re-evaluating the ion injection velocity from the presheath for maintaining steady-state quasineutrality.

In thermal, quiescent (not rf-driven) plasmas, the quasineutral presheath functions as a boundary, providing $\mathbf{B}$-aligned ion flow at the ion sound velocity c_s into the main sheath. The often-made assumption, extending the sonic flow injection to rf-driven sheaths, will be challenged by showing that a much lower ion injection velocity from the presheath

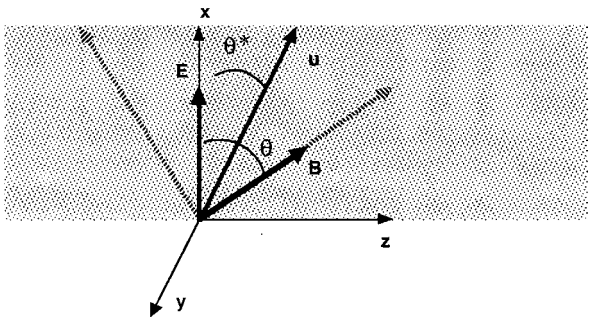

FIG. 1. Illustration of the field geometry and flow direction $\mathbf{u}$ of the ion guiding center motion.

is required to balance electron and ion currents. For the same reason the injection velocity along **B** turns out to be strongly dependent on the magnetic inclination relative to **E**.

In choosing the boundary conditions for the sheath equations one can prescribe either a sinusoidal current permeating the sheath or a sinusoidal externally applied voltage at the sheath boundaries. The first option has been favored in the past [1,2] because of its analytic simplicity. Given that the sheath formation is a nonlinear effect, a monochromatic (sinusoidal) current through the sheath leads to a sheath voltage with higher harmonics. In reality, it is usually the applied (driving) voltage that is monochromatic, inducing an anharmonic sheath current. Here, therefore, we elect a sinusoidal driving voltage as the boundary condition between the capacitor plates. That voltage equals the sum of the two sheath voltages, one on each plate, that are symmetric in space and 180° out of phase relative to each other. A coupled set of differential equations involving both sheaths is then obtained and solved numerically.

Three main conclusions follow from the study of the 1D magnetized coupled sheath model. (i) The scaling of the rectified sheath potential on the rf amplitude $V_{\rm rf}$ is nearly linear and similar to the sinusoidal current model. The sheath thickness, however, is somewhat smaller, scaling closer to $(eV_{\rm rf}/\kappa T_e)^{2/3}$ than to $(eV_{\rm rf}/\kappa T_e)^{3/4}$. (ii) The effect of oblique magnetic lines $\theta \neq 0$ is small at small θ but significant as **E** and **B** become orthogonal. The rectified sheath potential $V_{\rm dc}$ and the sheath thickness Δ increase as the magnetic angle increases. At a given magnetic angle, the increase in $V_{\rm dc}(\theta)/V_{\rm dc}(0)$ is higher for a higher ambient plasma density. (iii) The required ion injection velocity from the presheath is lower than the sound speed in order to maintain equal ion and electron fluxes. The strong dependence of the *B*-aligned injection velocity on the magnetic inclination is essential for the agreement between theory and earlier simulation results.

It is finally pointed out that the one-dimensional theory cannot address the effects from excitation of diocotron modes, having parallel wavelengths comparable to the sheath thickness and caused by the shear in the $\mathbf{E}\times\mathbf{B}$ drift. The effect of these two-dimensional modes is significant at large magnetic inclinations, causing drift velocity induced transport comparable to that obtained by acceleration across the sheath.

The remainder of this paper is organized as follows Section II introduces the basic adiabatic electron, fluid ion model and derives the coupled sheath equations in unmagnetized plasmas. A discussion of the magnetic field effects is given in Sec. III. The decoupling of the ion flow from the magnetic lines is parametrized by the introduction of the effective ion mass and the magnetized version of the sheath equations is subsequently derived. Section IV deals with the issue of quasineutrality, bearing into the ion injection velocity into the sheaths. The results are discussed in Sec. V and compared with earlier analytic models as well as numerical simulations. A summary of the results and conclusions appears in Sec. VI.

II. COUPLED EQUATIONS FOR SYMMETRICALLY DRIVEN rf SHEATHS

A uniform plasma placed between two parallel capacitor plates in the *yz* plane is considered. For the moment we assume a zero magnetic field in the plasma. An oscillating rf voltage is applied in the *x* direction between the plates

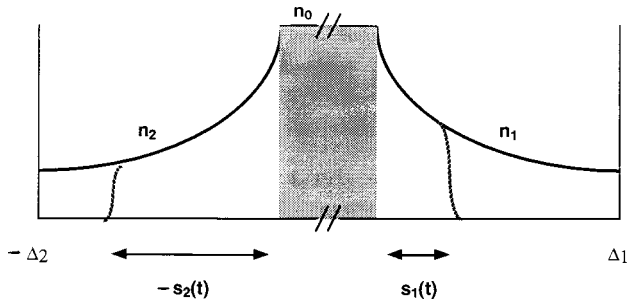

FIG. 2. Illustration of the sheath density profiles between the capacitor plates and the plasma.

$$\mathcal{V}_{\rm rf} = -V_{\rm rf}\cos(\omega t). \tag{1}$$

Adopting the one-dimensional approximation, for plate dimensions much longer than the sheath thickness, we assume that all quantities vary only in *x*. A cross section of the charge distribution across *x* is shown in Fig. 2. Within each sheath, the edge of the electron distribution $s(t)$ oscillates in time between the sheath plasma interface $s=0$ and the maximum sheath thickness $x=\Delta$, exposing a positive ion column of width $\Delta - s(t)$. Implicit in the above picture [1,2] is the assumption of adiabatic electrons and fluid ions: The local electron density is in thermal equilibrium with the instantaneous sheath potential, while the much slower ions respond to the time-averaged sheath potential. For that to occur the rf must be below the electron plasma and above the ion plasma and ion cyclotron frequencies,

$$\omega_e \gg \omega \gg \omega_i, \Omega_i, \tag{2}$$

In addition, the electron thermal velocity v_e must be much larger than the moving plate velocity.

$$v_e \gg \omega\Delta. \tag{3}$$

Finally, the steplike decay of the electron edge density is justified when the plasma Debye length $\lambda_D = \omega_e/\sqrt{\kappa T_e/m_e}$ is much smaller than the sheath thickness, satisfied if the applied rf voltage well exceeds the ambient plasma temperature $eV_{\rm rf} \gg \kappa T_e$.

Consider first the sheath on the right. For radio frequencies below the ambient plasma frequency and for electrostatic perturbations the electric field goes to zero for $x < s_1$. The instantaneous potential $\mathcal{V}_1(x,t)$ at any location inside the sheath is then given by

$$\mathcal{V}_1(x,t) = -4\pi \int_{s_1}^{x} dx' \int_{s_1}^{x'} dx'' \rho_1(x''), \quad x > s_1 \tag{4}$$

$$\mathcal{V}_1(x,t) = 0, \quad x \leqslant s_1. \tag{5}$$

The quasineutrality condition $n_e \simeq n_i$ applies behind each moving electron edge *s*. The total sheath charge density

$$\rho_{1,2}(x,t) = e[n_i(x) - n_e(x)] = 0, \quad x \leqslant s_{1,2}(t) \tag{6}$$

$$\rho_{1,2}(x,t) = en_i(x), \quad x > s_{1,2}(t), \tag{7}$$

is thus determined by the ion density profile n, henceforth dropping the subscript i. The total potential across each sheath is $V_{1,2}(t)\equiv\mathcal{V}_{1,2}(\Delta_1,t)$. Hence the total applied rf potential equaling the sum of $V_1(t)+V_2(t)$ is written as

$$-V_{\rm rf}\cos(\omega t)=-4\pi\int_{s_1}^{\Delta_1}dx'\int_{s_1}^{x'}dx''n_1(x'')+4\pi\int_{-\Delta_2}^{-s_2}dx'\int_{x'}^{-s_2}dx''n_2(x''). \quad (8)$$

Now, for symmetric sheath profiles, $n_1(x)=n_2(-x)$ and $\Delta_1=\Delta_2=\Delta$, the moving boundaries are 180° out of phase, $s_1(\phi)=-s_2(\phi+\pi)$; the symmetry $s_1(\phi)=s_1(-\phi)$ also implies $s_1(\phi)=-s_2(\pi-\phi)$.

The exact current through the discharge $J=j_i+j_e+\partial P/\partial t$ is approximated by the polarization current due to the oscillation of the sheath boundary $\dot{P}=(d/dt)\int_0^s dx\ \rho(x)$. The contribution from actual particle motion j_i and j_e is much smaller since the ion flow velocity is much slower than the sheath boundary, while electrons near thermal equilibrium behind the sheath boundary yield zero current [8]. The time derivative of Eq. (7) and the current equality in the plasma-sheath boundaries yields

$$J_1=\dot{s}_1n_1(s_1)=J_2=-\dot{s}_2n_2(s_2). \quad (9)$$

Though Eq. (9) is computed at each plasma-sheath boundary, it also gives the current at each plate by applying the conservation of $4\pi\mathbf{J}+\partial\mathbf{E}/\partial t$ for electrostatic oscillations $\boldsymbol{\nabla}\cdot(\boldsymbol{\nabla}\times\mathbf{B})=0$ and noticing that $\mathbf{E}$ is zero behind each sheath boundary and each plate surface. Taking the time derivative of Eq. (8) eliminates the integral signs [9] and yields an algebraic relation for the moving boundary velocity $\dot{s}_1$,

$$\omega V_{\rm rf}\sin(\omega t)=4\pi\dot{s}_1n_1(s_1)[(\Delta-s_1)+(\Delta-s_2)]=-4\pi\dot{s}_2n_2(s_2)[(\Delta-s_2)+(\Delta-s_1)]. \quad (10)$$

The motion of each sheath boundary is coupled to the charge contained in both sheaths; notice that $\dot{s}_1\neq-\dot{s}_2$ despite $J_1=J_2$.

When the rf is much higher than the characteristic ion frequencies $\omega\gg\omega_i,\Omega_i$ one can assume that perturbations on the rf time scale average out over the ion characteristic time and that the ions essentially respond to the time-averaged (rectified) sheath potential. Therefore, the sheath potential is split into dc and oscillating parts

$$\mathcal{V}_{1,2}(x,t)=U_{1,2}(x)+\tilde{\mathcal{V}}_{1,2}(x,t). \quad (11)$$

The time-averaged $U(x)=\langle\mathcal{V}(x,t)\rangle$ is obtained from the time-averaged Poisson equation

$$\frac{d^2U_{1,2}}{dx^2}=-4\pi\langle\rho_{1,2}(x,t)\rangle=-4\pi\frac{\omega\tau_{1,2}}{\pi}en_{1,2}(x), \quad (12)$$

where $\tau_{1,2}$ is the time when $s_{1,2}$ passes through x, i.e., $x=s_{1,2}(\tau_{1,2})$. The average charge density $\langle\rho\rangle$ is the ion density weighted by the time fraction that the ion column at x is exposed. The ion density profile then follows from the continuity equation at steady state

$$\frac{d}{dx}(n_{1,2}u_x)=0, \quad (13)$$

where u_x is determined by the ion motion in the rectified potential.

Assuming conservation of the ion cyclotron energy (invariance of magnetic moment), the energy balance across the sheath then yields the equation for u_x,

$$\tfrac{1}{2}m_iu_x^2+eU(x)=\tfrac{1}{2}m_iu_{0x}^2, \quad (14)$$

where the injection velocity of the presheath ions u_{0x} equals the ion-sound velocity $c_s=\sqrt{\kappa T_e/m_i}$. Solving Eq. (14) for u_x and substituting in the continuity equation (13) yields the ion density profile

$$n_{1,2}=\frac{n_0}{\sqrt{1+2eU_{1,2}(x)/m_iu_{0x}^2}}. \quad (15)$$

Equation (12) for the averaged sheath potential, Eq. (15) for the ion density, and Eq. (10) for the electron edge motion, supplemented with the boundary conditions $\mathcal{V}_0(0)=0$ and $d\mathcal{V}_0(0)/dx=E_0(0)\simeq0$, form a closed set of sheath equations. The first three combine into a dimensionless Poisson equation

$$\frac{d^2\overline{U}_1}{d\overline{x}^2}=-\overline{\rho}_1=-\frac{\phi(\overline{x})}{\pi}\frac{\overline{n}_1}{\sqrt{1+2\overline{U}_1(\overline{x})}}, \quad (16)$$

where $\overline{\mathcal{V}}=e\mathcal{V}_0/\kappa T_e$, $\overline{x}=x/\lambda_D$, $\overline{\rho}=\langle\rho\rangle/en_0$, and $\overline{n}=n_i/n_0$ with $1/\lambda_D^2=m_i\omega_i^2/\kappa T_i=4\pi e^2n_0/\kappa T_i$; we have assumed, without loss of generality that $T_e=T_i$. Here $\phi(\overline{x}_1)$ signifies the rf phase when the sheath boundary $s_1(t)$ is at x_1; since Eq. (10) is valid for every value x of s one obtains

$$\frac{d\phi}{d\overline{x}_1}=\frac{\overline{n}_1(\overline{x}_1)(2\overline{\Delta}-\overline{x}_1-\overline{x}_2)}{V_{\rm rf}\sin\phi}. \quad (17)$$

The equations for the left sheath follow by swapping indices 1 and 2 and taking into account that $\phi(\overline{x}_1)=\pi-\phi(\overline{x}_2)$. The x_1 integration in Eq. (16) proceeds until $\phi(x_1)$ in Eq. (17) reaches π; the $\overline{x}_1$ value there is the sheath thickness $\overline{\Delta}$ in units of λ_D.

The numerical solution of the sinusoidal voltage drive model yields the same linear dependence of the rectified sheath potential $V_{\rm dc}$ on the rf amplitude $V_{\rm rf}$ as the sinusoidal current drive model [1,2]. The sheath thickness, however, is found smaller than the sinusoidal current model. The detailed results from solving the unmagnetized equations of this section will be presented in Sec. IV as the parallel $\mathbf{B}$ limit of the magnetized sheath equations.

III. MAGNETIZED SHEATHS

The ion motion inside a magnetic field is a cyclotron rotation around a drifting guiding center (GC). In the fully magnetized ion picture the Larmor radius is much smaller than the sheath thickness $\rho_L = v_i/\Omega_i \ll \lambda_D = v_i/\omega_i$ and the guiding center motion is confined along the magnetic lines. The first assumption is satisfied for $eV_{\rm rf} \gg \kappa T_i$ given that the sheath thickness is then much larger than λ_D. However, in the case of oblique magnetic lines, the GC motion is really three dimensional and decouples from the magnetic lines due to the electrostatic gradient [7]. The term partially magnetized ions characterizes orbits of small Larmor radius that drift across the magnetic field and applies inside the sheath.

The orbit geometry is illustrated in Fig. 1, introducing a B_0-aligned coordinate system $(x_\perp, z_\parallel)$,

$$x = x_\perp \sin\,\theta + z_\parallel \cos\,\theta, \tag{18}$$

$$z = -x_\perp \cos\,\theta + z_\parallel \sin\,\theta. \tag{19}$$

In addition to the acceleration parallel to the magnetic field, there is the $\mathbf{u} \propto \mathbf{E}\times\mathbf{B}$ drift as well as an acceleration drift proportional to $d\mathbf{u}/\mathbf{d}t$ due to the variation of the $\mathbf{E}\times\mathbf{B}$ velocity. Though one needs only u_x to consider density variations in x, the full 3D solutions of the ion equations of motion are need to obtain u_x. Fortunately, in many cases, the motion described by the drift velocities depends on the field values at the instantaneous ion position, independent of time history. That being the case, one can eliminate other velocity components in favor of u_x, resulting in a constrained motion equation along x,

$$\tfrac{1}{2} m^*(\theta) u_x^2 + \mu B + eU(x) = \tfrac{1}{2} m_i u_{0_\parallel}^2 + \mu_0 B_0 \equiv \tfrac{1}{2} m_i u_0^2. \tag{20}$$

Here $u_\parallel$ represents the velocity of the ion GC, while the cyclotron rotation energy is given by μB. If the magnetic moment μ is an adiabatic invariant, for $u/L < \Omega$ where $L \simeq \Delta$ is the sheath scale length, the cyclotron energy is also invariant for constant B_0, dropping out of Eq. (20).

The effective mass $m^*(\theta)$ depends on the approximation. If one allows motion only along B, then from $u_z = u_x \tan\theta$ follows $m^*/m_i = 1 + \tan^2\theta = 1/\cos^2\theta$; moreover, the magnetic angle drops out of the sheath scaling [4,5]. That is valid only for $\mathbf{B}$ nearly parallel to $\mathbf{E}$. For fully 3D motion, exact solutions are possible [7] for a quadratic, constant charge density potential $U \propto m\omega_i^2 x^2$, yielding a constant flow angle relative to $\mathbf{B}$ and a constant effective mass $m^*(\theta) < m_B$ through the sheath. However, constant charge density results provide only scaling estimates [6] for the sheath behavior.

A general effective mass derivation, appropriate for an arbitrary sheath profile $U(x)$, is now introduced, based on the GC drift approximation. Strictly speaking, the drift equations are valid when the drift characteristic time is longer than the cyclotron period $ku_d \ll \Omega_i$ with $k = 1/\Delta$, which implies $\omega_i^2/\Omega_i^2 \ll 1$ for $u_d = eE/m\Omega_i \sim \omega_i^2\Delta/\Omega_i$. In Ref. [7], however, the *exact* solutions for motion under constant dE/dx demonstrated conservation of the gyroenergy with small Larmor radius $\rho/\Delta \ll 1$, for high $\omega_i^2/\Omega_i^2 \sim 1$ and high GC drift velocities. We conjecture that the adiabatic GC approximation is still valid for large and nonuniform gradients provided the variation dE/dx is monotonic (nonperiodic); the strength E_n of possible resonant harmonics $ku_d = n\Omega_i$ that might destroy adiabaticity is then negligible.

As ion acceleration along B shifts the x location [Eq. (18)] towards higher $E(x)$, the electron drift velocity, given by

$$u_y = -\sin\,\theta c E_0(x)/B_0, \tag{21}$$

also accelerates, introducing the inertial force $\mathbf{f} = -m d\mathbf{u}_y/dt$. The presence of the magnetic field causes a new drift $-c\mathbf{f}\times\hat{\mathbf{z}}_\parallel/eB$ to be orthogonal to the acceleration,

$$\mathbf{u}_\perp = \frac{m^2c^2}{e^2B^2}\frac{e}{m_i}\frac{dE_0}{dt}\sin\,\theta\hat{\mathbf{x}}_\perp = \frac{e}{m_i\Omega_i^2}\frac{d\mathbf{E}_\perp}{dt}. \tag{22}$$

Expression (22) is essentially a generalized polarization drift equation $u_\perp \equiv u_p$, with $dE_0/dt = \partial E_0/\partial t + (\dot{x}_\perp \sin\theta + \dot{z}_\parallel \cos\theta)(dE_0/dx)$. Setting $dE_0/dx = 4\pi e\overline{n}$ and $\partial E_0/\partial t = 0$ in Eq. (22) yields

$$u_\perp = \alpha u_\parallel, \quad \alpha = \frac{(\omega_i^2/\Omega_i^2)\overline{\rho}\sin\,\theta\,\cos\,\theta}{1-(\omega_i^2/\Omega_i^2)\overline{\rho}\sin^2\theta}. \tag{23}$$

Equation (23) relates $u_\perp$ to $u_\parallel$ [10] through the *local* electrostatic gradient, parametrized by $dE/dx/B^2 \propto (\omega_i^2/\Omega_i^2)\overline{\rho}$, with $\overline{\rho} = \langle\rho(x)\rangle/en_0$ the time-averaged sheath charge density and ω_i^2 the ambient ion plasma frequency. Substituting Eq. (23) in Eq. (18), it follows that the angle of motion relative to the x direction $u_z/u_x \equiv \tan\theta^* = (\sin\theta - \alpha\cos\theta)/(\cos\theta + \alpha\sin\theta) \equiv \tan(\theta - \tan^{-1}\alpha)$ is different from the magnetic angle $\tan\theta$. Eliminating u_z and using Eq. (21) for u_y, the energy conservation (20) yields the following equation of motion along x:

$$\frac{1}{2}m^*(\theta)u_x^2 + \left[\frac{1}{2}m_i\sin^2\theta\left(\frac{c}{B_0}\frac{dU}{dx}\right)^2 - eU(x)\right] = \frac{1}{2}m_i u_{0_\parallel}^2 = \frac{1}{2}m_B u_{0_x}^2, \tag{24}$$

where we have set $E_0 = -dU/dx$, assumed conservation of μ, expressed the presheath ion energy on the right-hand side via the fully magnetized mass $m_B/m_i = 1/\cos^2\theta$ given that $u_{0_x} = u_{0_\parallel}\cos\theta$, and defined the partially magnetized mass inside the sheath as

$$\frac{m^*(\theta)}{m_i} \equiv \sec^2\theta^* = \frac{1+\alpha^2}{(\alpha\,\sin\,\theta + \cos\,\theta)^2} \equiv \sec^2(\theta - \tan^{-1}\alpha). \tag{25}$$

The derived effective mass (25) differs from the constant charge density limit of Eq. 52 in Ref. [6] in that (i) $m^*(\theta)$ and θ^* vary across the sheath in response to the charge density variation $\overline{\rho}(x)$ and (ii) $m^*(\theta)$ absorbs the acceleration drift, but not the $\mathbf{E}\times\mathbf{B}$ drift, while the effective mass in Eq. 52 of Ref. [6] includes both drifts. Here the effective potential for the ion motion along $\mathbf{E}$ is the sheath potential minus the energy sunk into the $\mathbf{E}\times\mathbf{B}$ motion.

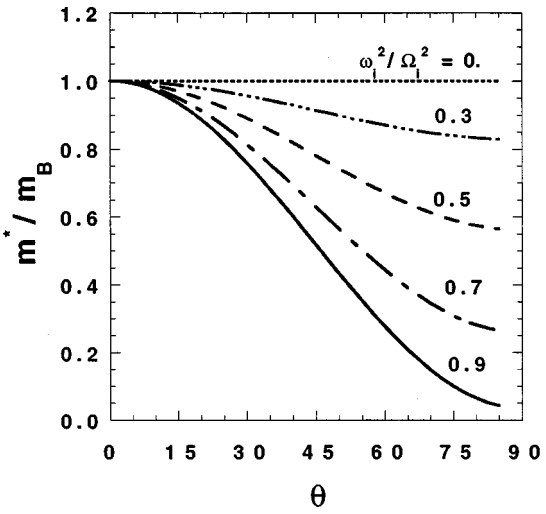

FIG. 3. Effective mass ratio m^*/m_B for the motion along **E** vs the magnetic angle θ. Different curves correspond to different values of ω_i^2/Ω_i^2. The $\omega_i^2/\Omega_i^2=0$ limit corresponds to completely magnetized $m_B=m^*$, regardless of the angle θ.

The magnetic field increases the inertia for x motion m^* since not all the sheath potential energy goes into ion acceleration across the sheath and thus m^* is always higher than m_i. On the other hand, m^* is less than the fully magnetized mass m_B because part of the acceleration drift points along the electric field (x direction). That is shown in Fig. 3, plotting the ratio m^*/m_B vs θ for various fixed ω_i^2/Ω_i^2. Compared to the earlier constant density results in Fig. 3 of Ref. [6], the ratios m^*/m_B are relatively higher for $\omega_i^2/\Omega_i^2 \leqslant 0.5$ and lower otherwise. For given magnetic angle θ, the flow angle θ^* changes across the sheath as the local gradient $dE/dx \propto \omega_i^2(\overline{x})$ changes since α in Eq. (23) depends on $\overline{\rho}(x)$. The difference $\theta^*-\theta$ between the flow and the magnetic angle increases deeper inside the sheath, as the ion flow increasingly tilts towards the electric field direction.

The presheath ions are magnetized since the electric field there is negligible and the injected ion flow is confined along the field lines $u_{x_0}=u_{0_\parallel}\cos\theta$. Combining Eq. (24) for the ion velocity v_x inside the sheath with the continuity equation (13) yields, after the usual normalizations [Eq. (16)], the ion density profile n_i^* for magnetized sheaths

$$\overline{n}_i^* = \frac{\overline{u}_{0_\parallel}\sqrt{m^*(\theta)/m_B}}{\sqrt{\overline{u}_{0_\parallel}^2+2\overline{U}-\sin^2\theta\left(\frac{\omega_i}{\Omega_i}\right)^2\left(\frac{d\overline{U}}{d\overline{x}}\right)^2}}. \tag{26}$$

Expression (26) goes to the unmagnetized n_i, Eq. (15) in the parallel **B** limit $\theta=0$. The magnetized version of Poisson's equation (16) becomes

$$\frac{d^2\overline{U}_1}{d\overline{x}_1^2} = -\frac{\phi(\overline{x}_1)}{\pi}\frac{\overline{u}_{0_\parallel}\sqrt{m^*(\theta)/m_B}}{\sqrt{\overline{u}_{0_\parallel}^2+2\overline{U}_1-\sin^2\theta\left(\frac{\omega_i}{\Omega_i}\right)^2\left(\frac{d\overline{U}_1}{d\overline{x}_1}\right)^2}} \tag{27}$$

and the sheath boundary motion is given by

$$\frac{d\phi}{d\overline{x}_1} = \frac{\overline{n}_1^*(\overline{x}_1)(2\overline{\Delta}-\overline{x}_1-\overline{x}_2)}{V_{\rm rf}\sin\phi}. \tag{28}$$

Cross-B drift effects manifest through the partial ion demagnetization $m^*/m_B \leqslant 1$ (acceleration drift along **E**) and the last term under the square root of Eq. (27), the $\mathbf{E}\times\mathbf{B}$ drift parallel to the plate. Notice that the effective potential under the square root becomes negative (retarding the ion x motion) at high electric gradients, meaning insufficient potential energy $U(x)$ to supply the $\mathbf{E}\times\mathbf{B}$ drift kinetic energy. That does not occur in reality because the GC drift approximation fails when the electric gradient length is comparable to the Larmor radius; the analytic model (22) is not accurate for $\omega_i^2/\Omega_i^2>1$. Exact calculations, albeit possible only for quadratic sheath potentials, show that no ion reflection takes place at large ω_i^2/Ω_i^2.

The flow angle $\theta^*(x)$ depends on the average sheath density $\overline{\rho}$ through Eq. (23) and $\overline{\rho}=(\phi/\pi)\overline{n}_i$ depends on θ^* through Eq. (26). Eliminating θ^* from Eqs. (23)–(26) yields the self-consistent ion density profile

$$\overline{n}_i^* = \overline{u}_{0_\parallel}\frac{\sqrt{1+\frac{\left(\frac{\omega_i}{\Omega_i}\right)^4\tau^2\sin^4\theta}{\overline{u}_{0_\parallel}^2+2\overline{U}_1-\sin^2\theta\left(\frac{\omega_i}{\Omega_i}\right)^2\left(\frac{d\overline{U}_1}{d\overline{x}}\right)^2-\left(\frac{\omega_i}{\Omega_i}\right)^4\tau^2\sin^2\theta}}-\sqrt{\frac{\left(\frac{\omega_i}{\Omega_i}\right)^4\tau^2\sin^4\theta}{\overline{u}_{0_\parallel}^2+2\overline{U}_1-\sin^2\theta\left(\frac{\omega_i}{\Omega_i}\right)^2\left(\frac{d\overline{U}_1}{d\overline{x}}\right)^2-\left(\frac{\omega_i}{\Omega_i}\right)^4\tau^2\sin^2\theta}}}{\sqrt{\overline{u}_{0_\parallel}^2+2\overline{U}_1-\sin^2\theta\left(\frac{\omega_i}{\Omega_i}\right)^2\left(\frac{d\overline{U}_1}{d\overline{x}}\right)^2-\left(\frac{\omega_i}{\Omega_i}\right)^4\tau^2\sin^2\theta}}, \tag{29}$$

in terms of the ambient plasma density ω_i^2/Ω_i^2, the injection velocity $\overline{u_{0_\parallel}} \equiv u_{0_\parallel}/c_s$, the ratio $\tau = \overline{u_{0_\parallel}}\phi(x)/\pi$, and the magnetic angle θ. Equations (27), (28), and (29) are the magnetized versions of Eqs. (16), (17), and (15); the latter are recovered at $\theta = 0$.

For thermal, quiescent (not rf-driven) sheaths the **B**-aligned ion injection velocity equals the sound speed [3] $\overline{u_{0_\parallel}} = 1$. That, however, is not valid for rf-driven sheaths. It is shown next that the ion injection speed parallel to the magnetic field is subsonic, with a strong dependence on the magnetic angle $u_{0_\parallel}(\theta) \leqslant c_s$.

We note in passing that if one were to fix $\overline{u_{0_\parallel}} = 1$, fix the effective ion mass $m^* \neq m_B$, and neglect the last term under the square root of Eq. (27), then $\overline{n_i^*} = \overline{n_i}(m^*/m_B)^{-1/2}$ and the magnetized equations rescale back the unmagnetized equations (15)–(17) by a length stretching $\overline{y} = (m^*/m_B)^{-1/4}\overline{x}$. Fixing the flow angle $\theta^* \neq \theta$ relative to **E** and neglecting the energy sunk into the parallel to the plate $\mathbf{E}\times\mathbf{B}$ drift would lead to the *same* total dc sheath voltage as in the unmagnetized case, distributed over a sheath thickness slightly expanded by a factor $(m^*/m_B)^{-1/4}$. Restoring the variable flow angle θ^* across the sheath and including the parallel to the plates $\mathbf{E}\times\mathbf{B}$ drift offers only marginal improvement towards the numerically observed strong magnetic influence. It is the introduction of the subsonic, θ-dependent, ion injection velocity below that yields full blown magnetic effects.

IV. CHARGE BALANCE WITH SUBSONIC ION INJECTION

While current conservation has been applied separately to the electron and ion fluxes through the sheaths, no provision has been made so far for *equating* the two fluxes to avoid violating the quasineutrality of the main plasma at steady state. In quiescent thermal sheaths balance occurs with the ion injection velocity greater than or equal to the ion sound speed $c_s = \sqrt{\kappa T_e/m_i}$ (Bohm condition). In rf-driven sheaths quasineutrality has usually been *assumed*, allowing ion injection along the magnetic lines with $u_{0_\parallel} = c_s$. Far from being automatically satisfied, the ion-electron flux balance must be invoked as a separate condition.

Imposing flux equality between electrons and ions requires adjusting the ion injection velocity from the presheath. While conservation in the ion current determines the ion density profile, the ambipolarity determines the ion injection velocity. It will be shown that flux balance requires subsonic ion injection velocities $u_{0_\parallel} < c_s$ that depend on the magnetic inclination.

While the ion flux is constant and equal to the presheath flux

$$j_i = j_{i0} = en_0 u_{0_\parallel}, \tag{30}$$

electrons arrive at the plates in ''spurts'' when the moving edge of the electron distribution $s(t)$ comes within a distance λ_d from the plate. From a total electron edge population equal to the ion edge density $n_i(\Delta)$ (Fig. 2) only those with velocity $u_e = \sqrt{2(\mathcal{E}-V)/m_e}$ above the sheath potential barrier will strike the plate. Applying Maxwell-Boltzmann statistics yields the instantaneous electron current as

$$j_e(\phi) \simeq en_i(\Delta)\int_{V(\phi)}^{\infty} d\mathcal{E}\,\frac{1}{m_e}\,\sqrt{\frac{m_e}{2\pi\kappa T_e}}\,e^{-\mathcal{E}/\kappa T_e}$$

$$\simeq en_i(\Delta)\sqrt{\frac{kT_e}{2\pi m_e}}\,e^{-eV(\phi)/\kappa T_e}, \tag{31}$$

where $\mathcal{E}$ is the total electron energy. Setting

$$V[s = s(\phi)] \simeq \tfrac{1}{2}\, m_i\omega_i^2\overline{n_i}(\Delta)s^2(\phi) \tag{32}$$

and approximating the sheath boundary motion $s(\phi)$ near the plate as

$$s(\phi) \simeq \frac{\Delta}{2}\,(1-\cos\,\phi) \simeq \frac{\Delta}{4}\,\phi^2 \tag{33}$$

obtains

$$j_e(\phi) \simeq en_i(\Delta)\sqrt{\frac{kT_e}{2\pi m_e}}\,e^{-\gamma\phi^4}, \tag{34}$$

with $\gamma = \overline{n_i}(\Delta)m_i\omega_i^2\Delta^2/32\kappa T_e$. Averaging over an ac period yields

$$\overline{j_e} \equiv \frac{1}{2\pi}\int_{-\pi}^{\pi} d\phi\; j_e(\phi) = \frac{1}{\pi}\,\frac{\Gamma(\frac{1}{4})}{4\gamma^{1/4}}\,\sqrt{\frac{kT_e}{2\pi m_e}}\,en_i(\Delta), \tag{35}$$

where $\Gamma(\frac{1}{4})/4 = 0.906$ and the ϕ integration was extended to $\pm\infty$ because of the rapid decay in the exponential (34). Equating $\overline{j_e}$ with the ion flux (30) yields

$$u_{0_\parallel} = \frac{\Gamma(\frac{1}{4})}{4\pi}\left(\frac{32\kappa T_e}{m_i\omega_i^2\Delta^2}\right)^{1/4}\sqrt{\frac{kT_e}{2\pi m_e}}\,\overline{n_i}(\Delta)^{3/4}. \tag{36}$$

Since both sides are functions of θ, dividing Eq. (36) by its $\theta = 0$ limit and using Eq. (26) for n_i yield

$$\frac{u_{0_\parallel}(\theta)}{u_{0_\parallel}(0)} = \left(\frac{n_\Delta(\theta)}{n_\Delta(0)}\right)^3\left(\frac{\Delta(0)}{\Delta(\theta)}\right)^2$$

$$\simeq \left(\frac{m^*(\theta)}{m_B}\right)^{3/2}\left(\frac{2V_{\rm dc}(0)}{2V_{\rm dc}(\theta)}\right)^{3/2}\left(\frac{\Delta(0)}{\Delta(\theta)}\right)^2. \tag{37}$$

It follows that the ion injection velocity *along the magnetic lines* depends on the angle θ. Two factors restrict the electron flux to the plates for a rf-driven sheath, relative to a thermal sheath. First, the electron density at the edge is limited by the large extent of the sheath $\Delta \gg \lambda_e$, as shown in Fig. 2. Second, the electron edge touches the wall only for a small fraction $\sim\lambda_e/\Delta \ll 1$ of the rf period. The ion current flux is then proportionally restricted to maintain quasineutrality in the main plasma volume.

It is the dependence of the ion injection velocity on the magnetic angle that yields the main effect on the induced sheath voltage and thickness. A thoroughly self-consistent approach requires solving the sheath equations (27)–(29) with Eq. (36) as the boundary velocity. That is rather involved numerically because the desired boundary value $V_{\rm dc} \equiv U(\Delta)$ is also a parameter in the equations to be solved

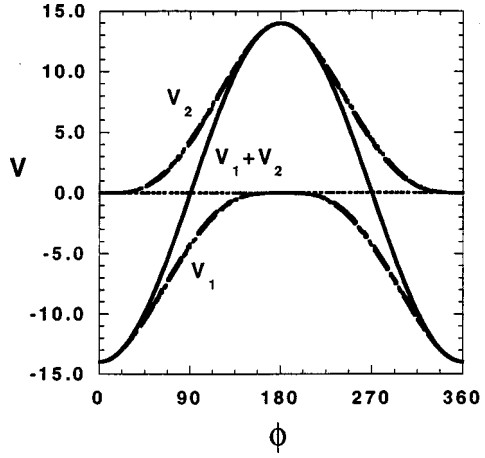

FIG. 4. Oscillating voltages (normalized to $\kappa T_e/e$) vs the rf phase at each sheath (dashed line) and the total voltage across the plates (solid line), the sum of the sheath voltages. Here $\omega_i^2/\Omega^2=1$ and the applied $V_{\rm rf}=14$. The sheath voltages obtained for three magnetic angles $\theta=0°,45°,75°$ (heavy dotted lines) are practically indistinguishable. The difference from the applied sinusoidal voltage (light dotted lines) is of the numerical accuracy order.

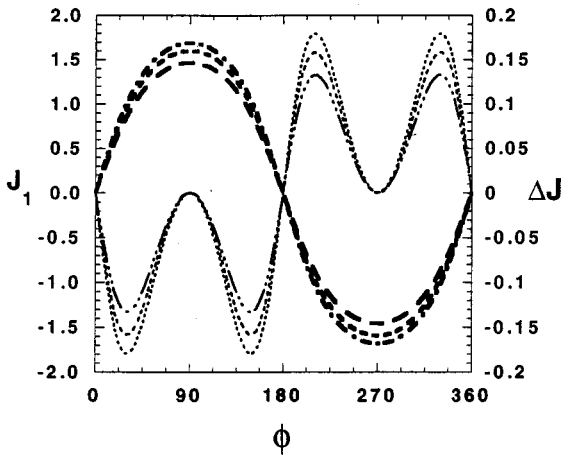

FIG. 5. Sheath current vs phase (heavy dashed lines) for three different magnetic angles, as in Fig. 4, at the applied $V_{\rm rf}=14$. The anharmonic current component, i.e., the difference $J(\phi)-J_{mx}\sin\phi$, is shown by light dashed lines.

[entering through $n_i(\Delta)$ in Eqs. (36) and (15)] and will not be attempted. Instead the approximation

$$u_{0_\parallel}(\theta)\simeq c_s\left(\frac{m^*(\theta)}{m_B}\right)^{3/2} \tag{38}$$

is employed in the subsequent results, neglecting the weaker θ dependence of Δ and $V_{\rm dc}$ in Eq. (37). The effective mass ratio is given by Eqs. (23) and (25), using the average charge density $\overline{\rho}(\Delta)=\phi(\Delta)/\pi n_i(\Delta)=n_i(\Delta)$ from Eq. (29), with the empirical relations $\overline{U_1}(\Delta)\equiv V_{\rm dc}=0.4V_{\rm rf}$, $d\overline{U_1}/dx|_\Delta = E_1(\Delta)\simeq 2V_{\rm dc}/\Delta$, and $\Delta=1.6V_{\rm rf}^{0.6}$.

V. RESULTS

Equations (27)–(29) cannot be analytically integrated. They are solved numerically using standard ''shooting'' techniques for two-point boundary problems. A complication arises from the fact that one of the boundary values, the sheath thickness Δ, also appears as a coefficient of the differential system, which cannot be readily handled by existing solvers. The difficulty is circumvented by introducing $\overline{x}^*_{1,2}\equiv\Delta-\overline{x}_{1,2}$ as a new independent variable and solving simultaneously an expanded system with two additional differential equations for $d\overline{x}^*_{1,2}/d\phi=-d\overline{x}_{1,2}/d\phi$ (see the Appendix).

The oscillating sheath voltages $V_{1,2}(t)$ obtained are plotted in Fig. 4. The total plate voltage, the sum V_1+V_2, given by the solid dotted curve, is practically indistinguishable from the exact applied plate potential. By contrast, the sheath voltage solutions under sinusoidal sheath current yield higher harmonic components in the plate voltage, of amplitude above 10% of the fundamental. Here it is the sheath current, shown in Fig. 5, that is anharmonic with higher harmonic content of the order 10%.

The time-averaged (dc) profiles for the voltage and electric field inside a sheath are shown in Fig. 6. The light dotted curves are the best fitting curves proportional to x^q. The power exponents are $q=7/3$ and 4/3 for U_0 and E_0, respectively, and change little with the external rf amplitude. What changes is the total sheath dc potential $V_{\rm dc}=U_0(\Delta)$, the dc field at the plate $E_{\rm dc}=E_0(\Delta)$, and the sheath thickness Δ. They are shown, respectively, in Figs. 7(a) and 7(b) against the rf amplitude $V_{\rm rf}$. A simple power law $aV_{\rm rf}^p$ fits fairly well with the results where $a=0.40$ and $p=1.0$ for $V_{\rm dc}$ and $a=1.23$ and $p=0.61$ for Δ. The almost linear dependence of $V_{\rm dc}$ on $V_{\rm rf}$ is similar to that under the sinusoidal current drive; the asymptotic slope 0.40 is also near the 0.43 previous theory limit. However, the sheath thickness $\Delta/\lambda_d=1.23(eV_{\rm rf}/\kappa T)^{0.6}$ is smaller than the sinusoidal current result $\Delta/\lambda_d=3.39(eV_{\rm rf}/\kappa T)^{3/4}$.

The magnetic field effects are investigated by considering oblique **B** relative to **E**, $\theta\neq 0$. The dc sheath voltage and the sheath thickness curves, shown in Figs. 7(a) and 7(b) for $\theta=45°$ and 75°, maintain the same power dependence on the rf amplitude as for $\theta=0°$. The slope, however, increases to

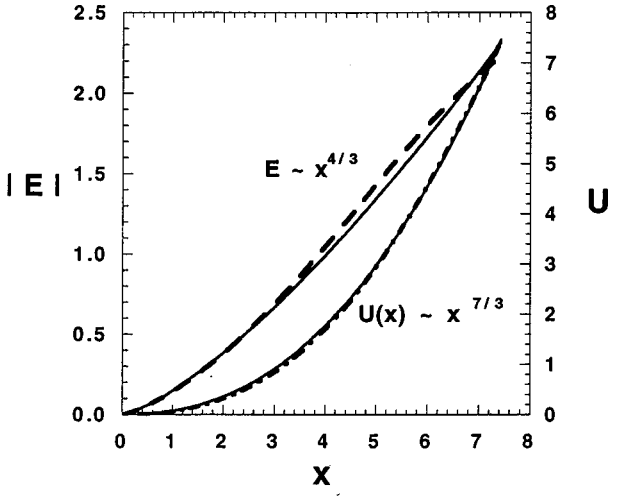

FIG. 6. Time-averaged (dc) voltage $\overline{U}=eU/\kappa T_e$ and electric field $|\overline{E}|$ profiles vs the distance x/λ_D across the left sheath. Here $\omega_i^2/\Omega^2=0.5$, $\theta=75°$, and $V_{\rm rf}=14$. The light curves are best fitting power laws.

$a=0.53$ for V_{dc} and $a=1.41$ for Δ. The exact θ dependence under a given V_{rf} will be given later.

The ion flow angle θ^*, which is equal to the magnetic angle θ at the presheath, gradually tilts towards the **E** direction as ions move deeper in the sheath, as illustrated in Fig. 8. The sheath voltage profiles $U(x)$ for a given rf amplitude are plotted in Fig. 9(a) for various magnetic angles. The profiles are similar except that the sheaths extend to longer distances and higher voltages with increasing θ. The corresponding ion density profiles and the time-averaged total charge densities are shown in Fig. 9(b). The total charge density rises quickly from zero near the plasma interface to a nearly constant value, equal to the ion density at the sheath edge (plate). Notice how the difference $\theta^*-\theta$ relates to the charge density buildup $dE/dx \propto \rho$, according to Eqs. (23)–(25). The approximate constancy of the charge density justifies the quadratic sheath approximation that has been used earlier to scale sheaths obtained from numerical simulations.

The ion ''demagnetization'' enhances the decrease in the ion density at the wall by a factor of $[m^*(\theta)/m_B]^{-1/2}$ compared to the unmagnetized $\theta=0$ case. The subsequent decrease in the electron edge density touching the wall (Fig. 2) further restricts the electron current through the sheath. In response, the ion injection velocity along **B** from the

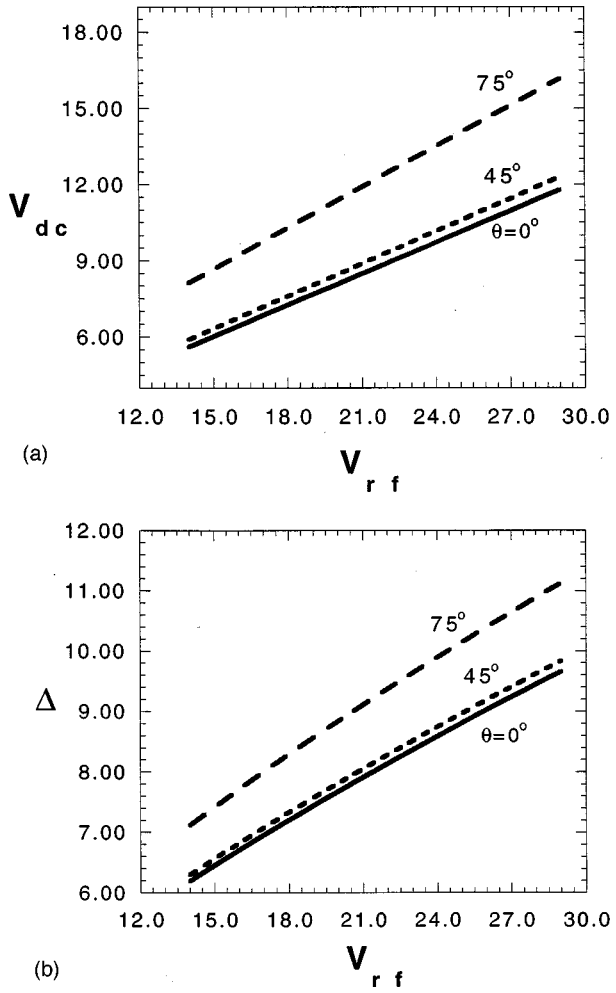

FIG. 7. Rectified (a) sheath voltage $V=eV_{dc}/\kappa T_e$ and (b) sheath thickness Δ/λ_D vs the applied rf amplitude for $\omega_i^2/\Omega_i^2=0.5$ at various magnetic angles as marked.

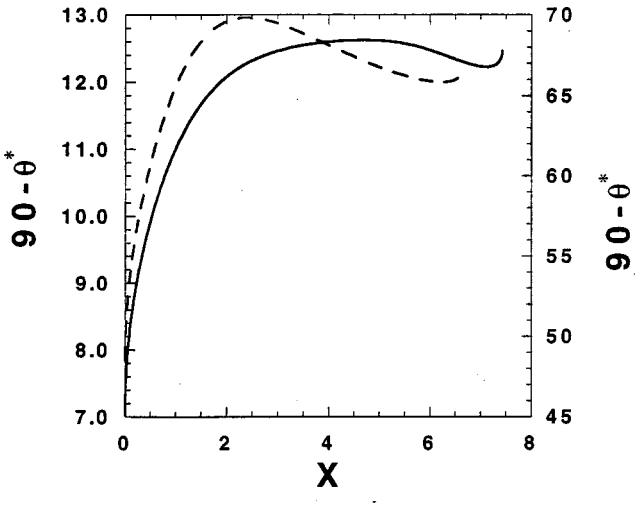

FIG. 8. Change in the ion flow angle θ^* across the sheath at large $\omega_i^2/\Omega_i^2=2$ for two different magnetic angles $\theta=83°$ (solid line) and $\theta=45°$ (dashed line), showing flow slippage from the magnetic lines and gradual tilting towards the **E** field.

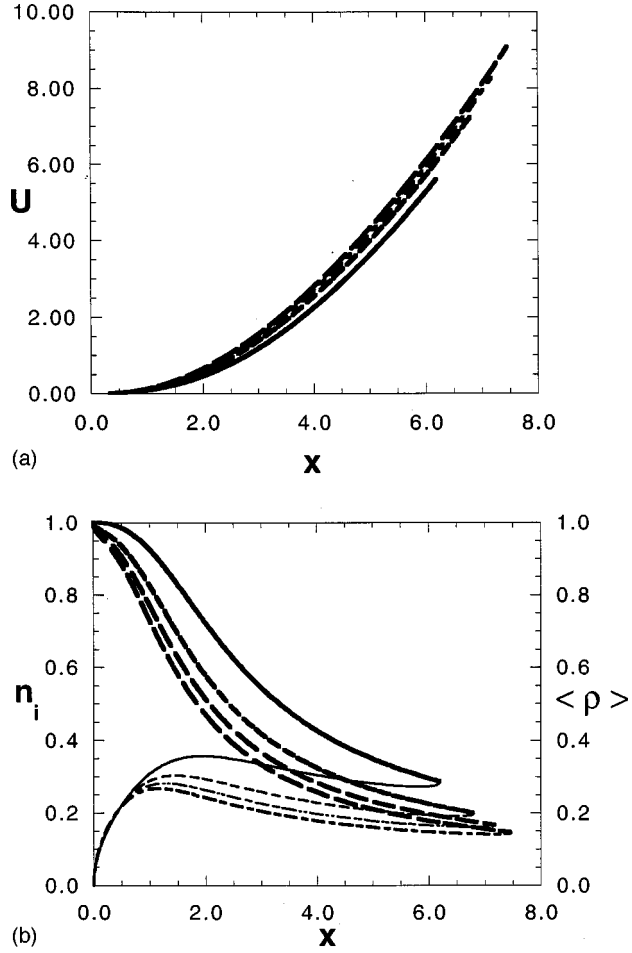

FIG. 9. Typical (right sheath) profiles for magnetic angles $\theta=0°,45°,60°,75°$. (a) Potential $eU/\kappa T_e$ vs the sheath position x/λ_e (from bottom to top). (b) Ion density profiles $\overline{n_i}(x)$ (heavy curves, from top to bottom) and the time-averaged charged density $\overline{\rho}(x)$ (light curves). Here $\omega_i^2/\Omega_i^2=0.33$. The sheath thickness is different for each case.

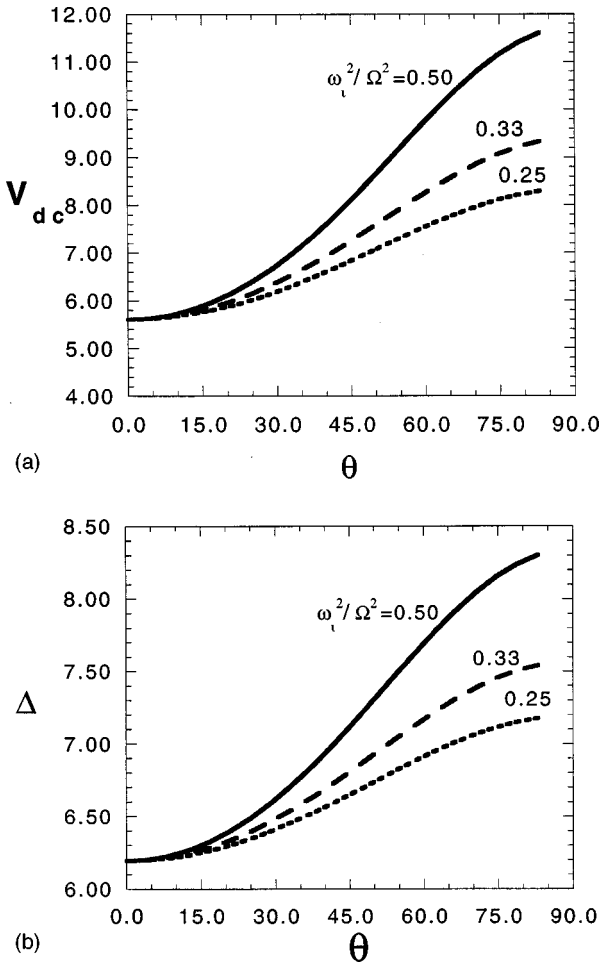

FIG. 10. Rectified (a) sheath voltage $eV_{dc}/\kappa T_e$ and (b) sheath thickness Δ/λ_D vs the external magnetic angle θ for the constant applied rf amplitude $eV_{rf}/\kappa T_e=14$ and various ambient plasmas ω_i^2/Ω_i^2 as marked.

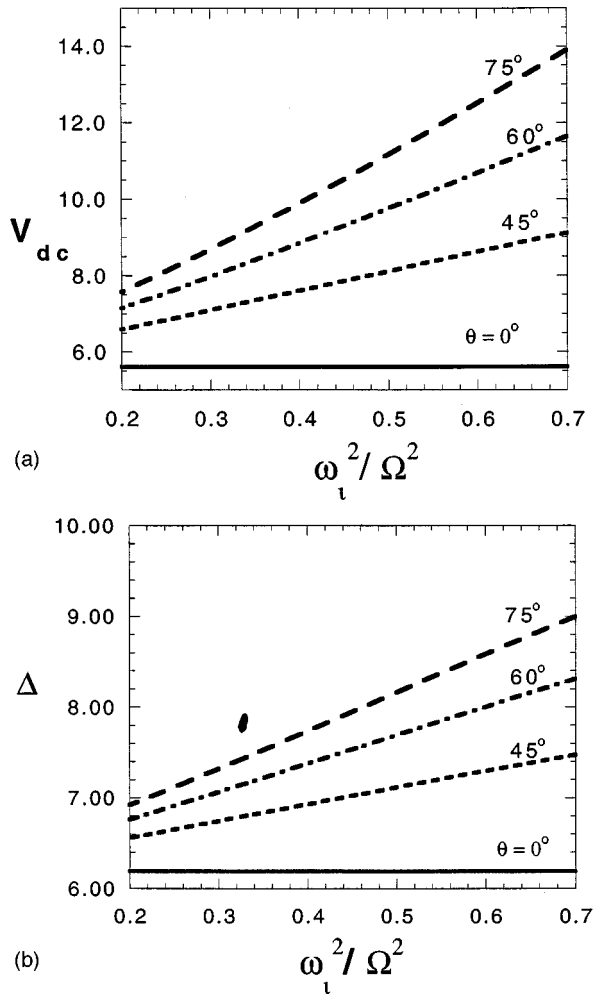

FIG. 11. Rectified (a) sheath voltage $eV_{dc}/\kappa T_e$ and (b) sheath thickness Δ/λ_D vs the ambient plasma ω_i^2/Ω_i^2 for the constant applied rf amplitude $eV_{rf}/\kappa T_e=14$ and various external magnetic angles as marked.

presheath is also reduced, relative to the unmagnetized limit, to maintain flux balance. The combined effect leads to the dependence of the sheath voltage and the sheath thickness Δ on the magnetic angle, plotted respectively in Figs. 10(a) and 10(b); various curves correspond to various ambient plasma densities. Both the dc potential and sheath thickness under a given rf strength increase with increasing magnetic angle; the increase is rather uniform with the magnetic angle. At a given angle the magnetic effects become stronger with increasing ambient density, parametrized by ω_i^2/Ω_i^2, as shown in Figs. 11(a) and 11(b).

The analytic results are compared to particle simulation results [6] in Fig. 12, plotting the increase in sheath voltage $V_{dc}(\theta)/V_{dc}(0)$ vs the magnetic angle. The best agreement is observed at ambient plasma density $\omega_i^2/\Omega_i^2=0.33$. Earlier approximate scaling theory [6] yields similar agreement with the simulations for $\omega_i^2/\Omega_i^2=0.45$. The steady-state ambient plasma density in these simulations is not known, but it is definitely smaller than the initial fill density of $\omega_i^2/\Omega_i^2=0.75$. Notably, both the present theory and the earlier scaling results are obtained by invoking electron-ion flux balance.

That using the consistent subsonic θ-dependent ion injection velocity is essential for agreement with simulations is demonstrated by the theoretical results of Fig. 13, obtained for fixed $u_{0_\parallel}=c_s$ as the boundary condition. There the sheath voltage vs the magnetic angle [Fig. 13(a)] remains practically constant and the increase in the sheath thickness is only

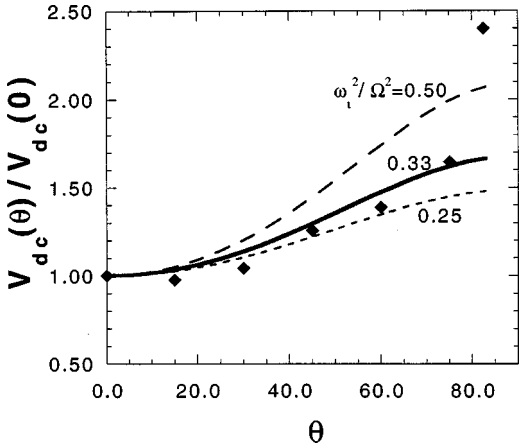

FIG. 12. Rectified sheath voltage vs the magnetic angle, normalized to the unmagnetized (parallel) limit $V_{dc}(\theta)/V_{dc}(0)$. Diamonds show the particle simulation results taken from [6].

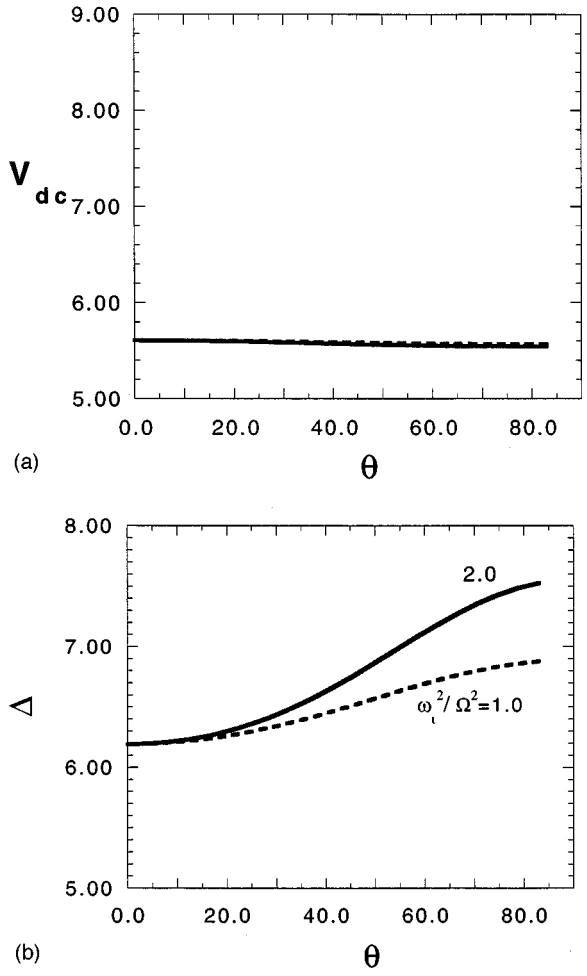

FIG. 13. Same as in Fig. 10, but with a fixed ion injection velocity equal to c_s.

marginal [Fig. 13(b)] despite the use of higher ambient plasma densities than in Figs. 9–12.

VI. CONCLUSIONS

The usual 1D sheath model, based on fluid ions and thermalized electrons, has been generalized by including the effects from oblique magnetic fields, redefining the ion injection velocity to preserve charge neutrality in the ambient plasma, and applying sinusoidal voltage boundary conditions. The magnetized presheath ions get partially demagnetized inside the sheath and their motion is not constrained along the magnetic lines. The ion GC drifts, stemming from the electric field gradient, are incorporated in the effective ion mass. The solutions for sinusoidal voltage boundary conditions are obtained numerically by solving the coupled equations for two symmetric sheaths.

It was found that an applied harmonic voltage drives an anharmonic current through the sheath (earlier results assuming harmonic sheath current find an anharmonic sheath voltage). The scaling of the rectified sheath potential on the rf amplitude is nearly linear and similar to the sinusoidal current model. The sheath thickness, however, is somewhat smaller, scaling closer to $(eV_{\rm rf}/\kappa T_e)^{2/3}$ rather than $(eV_{\rm rf}/\kappa T_e)^{3/4}$.

The effects of oblique magnetic lines $\theta \neq 0$ increase with increasing angles between **E** and **B**. Both the rectified sheath potential $V_{\rm dc}$ and the sheath thickness Δ increases significantly under a given rf amplitude as the angle gets closer to orthogonal. For a given magnetic angle θ the effects get stronger with increasing ambient plasma density, meaning an increased sheath charge density. The unmagnetized plasma results are recovered at the parallel magnetic field limit $\theta = 0$.

It is also argued, on grounds of sustaining the ambient plasma quasineutrality, that the ion injection velocity from the presheath must be less than the sound speed. The sheath potential is sensitive to the dependence of the **B**-aligned ion injection velocity on the magnetic inclination θ. Use of the sound speed for injection causes an underestimation of the magnetic angle effects on the induced sheath voltage.

The development of a two-dimensional sheath theory seems essential to improve further the description of magnetized sheaths. The shear in the $\mathbf{E}\times\mathbf{B}$ ion velocity is known to excite diocotron-type instabilities with finite wave number parallel to the surface. Electron transport is then determined by a two-dimensional potential, particularly in cases of nearly orthogonal **E** and **B**. The saturation level of diocotron modes can be as high as the applied rf potential, significantly changing the sheath profile. For example, the increase in the sheath potential at $\theta > 80°$ under a given rf drive, documented in the numerical particle-in-cell simulations of Fig. 12, cannot be accounted for by the magnetized 1D theory presented here.

ACKNOWLEDGMENT

This work was partially supported by the Department of Energy under Grant No. DE-FG05-49ER54201.

APPENDIX: SHEATH EQUATIONS FOR NUMERICAL INTEGRATION

To solve Eqs. (27)–(29) numerically, the second-order equation for the time-averaged sheath potential U_1 is replaced by

$$\frac{d\overline{U_1}}{d\phi} = \frac{d\overline{U_1}}{d\overline{x_1}}\frac{d\overline{x_1}}{d\phi} = -\overline{E_1}\,\frac{V_{\rm rf}\sin\phi}{\overline{n(x_1)}(\Delta - x_1 + \Delta - x_2)}, \tag{A1}$$

$$\frac{d\overline{E_1}}{d\phi} = \frac{d\overline{E_1}}{d\overline{x_1}}\frac{d\overline{x_1}}{d\phi} = \frac{\phi}{\pi}\,\overline{n(x_1)}\,\frac{V_{\rm rf}\sin\phi}{\overline{n(x_1)}(\Delta - x_1 + \Delta - x_2)}. \tag{A2}$$

Exploiting the symmetry between the left and right sheaths $\phi(\overline{x_2}) = \pi - \phi(\overline{x_1})$, the left sheath equations are

$$\frac{d\overline{U_2}}{d\phi} = \frac{d\overline{U_2}}{d\overline{x_2}}\frac{d\overline{x_2}}{d\phi} = -\overline{E_2}\,\frac{V_{\rm rf}\sin\phi}{\overline{n(x_2)}(\Delta - \overline{x_2} + \Delta - \overline{x_1})}, \tag{A3}$$

$$\frac{d\overline{E_2}}{d\phi} = \frac{d\overline{E_2}}{d\overline{x_2}}\frac{d\overline{x_2}}{d\phi} = \frac{\pi - \phi}{\pi}\,\overline{n(x_2)}\,\frac{V_{\rm rf}\sin\phi}{\overline{n(x_2)}(\Delta - \overline{x_2} + \Delta - \overline{x_1})}. \tag{A4}$$

The time-averaged sheath potential $\overline{U}_{1,2}$ and electric field $\overline{E}_{1,2}$ are now given as functions of the rf phase $0 \leqslant \phi \leqslant \pi$ through the relations

$$\frac{d\overline{x_1}}{d\phi} = \frac{V_{\rm rf}\sin\,\phi}{\overline{n}(\overline{x_1})(\Delta - \overline{x_1} + \Delta - \overline{x_2})}, \tag{A5}$$

$$\frac{d\overline{x_2}}{d\phi} = \frac{V_{\rm rf}\sin\,\phi}{\overline{n}(\overline{x_2})(\Delta - \overline{x_1} + \Delta - \overline{x_2})}, \tag{A6}$$

Using the density profile given in Eqs. (29), Eqs. (A1)–(A6) are six differential equations with six unknowns $\overline{U}_{1,2}$, $\overline{E}_{1,2}$, and $\overline{x}_{1,2}$, subject to the following boundary conditions: $\overline{U}_1(0)=0$, $\overline{E}_1(0)=0$, $\overline{x}_1(0)=0$, $\overline{U}_2(\pi)=0$, $\overline{E}_2(\pi)=0$, and $\overline{x}_2(\pi)=0$.

Observe that the integrand on the right-hand sides of Eqs. (A1)–(A6) is an explicit function of the boundary value $\overline{\Delta} \equiv \overline{x}_1(\phi=\pi) = \overline{x}_2(0)$, a peculiarity that cannot be readily handled by the existing differential solvers. To circumvent that difficulty, one can introduce

$$\overline{x}_1^* \equiv \overline{\Delta} - \overline{x}_1, \tag{A7}$$

$$\overline{x}_2^* \equiv \overline{\Delta} - \overline{x}_2, \tag{A8}$$

as independent variables subject to the differential equations

$$\frac{d\overline{x}_1^*}{d\phi} = -\frac{d\overline{x}_1}{d\phi}, \tag{A9}$$

$$\frac{d\overline{x}_2^*}{d\phi} = -\frac{d\overline{x}_2}{d\phi} \tag{A10}$$

and the boundary conditions $\overline{x}_1^*(\pi)=0$ and $\overline{x}_2^*(0)=0$. Together with the original equations (A1)–(A6), Eqs. (A9) and (A10) form a system of eight equations with eight unknowns $\overline{U}_{1,2}$, $\overline{E}_{1,2}$, $\overline{x}_{1,2}$, and $\overline{x}_{1,2}^*$. The boundary condition Δ does not appear explicitly (it has been absorbed inside $\overline{x}^*$) and the equations are solved using a standard ''shooting'' integrator.

[1] V. A. Godyak and N. Sternberg, Phys. Rev. A **42**, 2299 (1990).

[2] M. A. Lieberman, IEEE Trans. Plasma Sci. **16**, 638 (1988).

[3] R. Chodura, Phys. Fluids **25**, 1628 (1982).

[4] F. W. Perkins, Nucl. Fusion **29**, 575 (1989).

[5] J. R. Myra, D. A. D'Ippolito, and M. J. Gerver, Nucl. Fusion **30**, 845 (1990).

[6] S. Riyopoulos, Phys. Plasmas **3**, 2511 (1996).

[7] S. Riyopoulos, Phys. Plasmas **3**, 4355 (1996).

[8] For a fixed boundary, the incoming electron velocity equals the reflected and the incoming electron flux equals the reflected yielding zero net current. For a receding boundary, electrons are reflected with smaller velocity than the impacting velocity; the difference equals twice the velocity of the moving boundary. Taking one-half of the current just behind and just in front of the moving boundary (the latter is zero), the lowest-order kinetic electron description yields the same result as the polarization current (9).

[9] One can write $\int_{s_1}^{\Delta_1} dx' \int_{s_1}^{x'} dx'' \rho_1(x'') = \int_{s_1}^{\Delta_1} dx' F(s_1,x')$, where $F(s_1,x') = \int_{s_1}^{x'} dx'' \rho_1(x'')$ and the time dependence is in $s_1(t)$. The time derivative yields $-\dot{s}_1 F(s_1,s_1) + \int_{s_1}^{\Delta_1} dx' \dot{F}(s_1,x') = -\int_{s_1}^{\Delta_1} \dot{s}_1 n(s_1) dx' = -\dot{s}_1(\Delta - s_1)\rho_1(s_1)$, observing that $F(s_1,s_1)=0$. The same result is obtained by applying the identity $\int_{s_1}^{\Delta_1} dx' \int_{s_1}^{x'} dx'' \rho_1(x'') = \int_{s_1}^{\Delta_1} dx' (\Delta - x')\rho(x')$ before differentiating.

[10] Here a space-varying field $dE_0/dx \neq 0$, $\partial E_0/\partial t = 0$ yields a relation between u_p and $u_\parallel$, while the most frequently addressed time-varying field $dE_0/dx = 0$, $\partial E_0/\partial t \neq 0$ yields the value u_p directly. Also, a uniform time variation $\partial E_0/\partial t = \text{const}$ yields a constant u_p, while a uniform spatial variation $dE_0/dx = \text{const}$ yields an accelerated polarization drift.